Available online at www.sciencedirect.com
ScienceDirect
Trans. Nonferrous Met. Soc. China 34(2024) 157−170
Transactions of Nonferrous Metals Society of China
www.tnmsc.cn

Superior corrosion resistance and thermal/electro properties of graphene−epoxy composite coating on Mg alloy with biomimetic interface and orientation

Pu-sheng SUI[1], Cheng-bao LIU[1], Ai-meng ZHANG[1], Cong SUN[1], Lan-yue CUI[1], Rong-chang ZENG[1,2]

1. College of Materials Science and Engineering, Shandong University of Science and Technology, Qingdao 266590, China;
2. School of Materials Science and Engineering, Zhengzhou University, Zhengzhou 450002, China

Received 4 October 2022; accepted 19 May 2023

Abstract: Biomimetic graphene−epoxy composite coating was fabricated with a "brick and mud" structure via a spin-coating strategy. Imidazolium-based ionic liquids modified graphene (GI) was synthesized to improve the interfacial compatibility between the graphene (G) layers and epoxy resin. The surface morphology and chemical structures were observed and analyzed through scanning electron microscopy (FE-SEM), Raman spectroscopy, and X-ray photoelectron spectroscopy (XPS) as well as Fourier transform infrared spectroscopy (FTIR). The thermal imager was used to record the temperature change on the surface. The surface resistivity and thermal conductivity of the coating were determined via volumetric surface area resistivity tester and laser flash method, respectively. The corrosion resistance was investigated through electrochemical impedance spectroscopy (EIS) and salt spray testing. The GI layers in the composite coating exhibited a near-parallel orientation, which led to improved heat transfer and electrostatic dissipative efficiency. The through-plane thermal conductivity and surface resistivity were 0.77 $W \cdot m^{-1} \cdot K^{-1}$ and $1.6 \times 10^6\ \Omega \cdot cm$, respectively. Electrochemical impedance spectroscopy tests revealed that the low-frequency modulus of the coating reached $6.76 \times 10^{10}\ \Omega \cdot cm^2$ after 40 d of immersion, which was about two orders of the magnitude higher than that of the pure epoxy coating, showing a superior corrosion resistance.

Key words: biomimetic structure; composite coating; magnesium alloy; graphene orientation; corrosion resistance

1 Introduction

Magnesium (Mg) and its alloys have attracted great attention in automobile, aerospace, 5th-generation mobile communication and electronic industries due to their lightweight, high specific strength, good electrical and thermal conductivity, and excellent electromagnetic shielding properties as well [1−3]. However, the poor corrosion resistance of Mg alloys impedes their practical applications [4]. Surface modifications such as chemical conversion coatings [5], layered double hydroxide (LDH) [6], layer-by-layer (LBL) self-assembly [7], electroless plating [8], and sol−gel [9] together with micro-arc oxidation (MAO) have been extensively employed to improve the anticorrosion performance of Mg alloys. The disadvantage of chemical conversion coatings is the weak bonding of the coating to its substrate. The LDH coating needs a time-consuming process. And LBL-assembly processing can deteriorate the Mg substrate. Electroless plating has the advantages of high yield and low cost, but the magnesium alloy is subject to corrosion in the plating solution and susceptible to galvanic corrosion with the plated metal [10]. Sol−gel coatings can promote the formation of chemical bonding between the coating

Corresponding author: Rong-chang ZENG, Tel: +86-18754280969, E-mail: rczeng@foxmail.com;
Cheng-bao LIU, Tel: +86-15669239619, E-mail: chengbaocl@163.com
DOI: 10.1016/S1003-6326(23)66388-5

and its substrate. However, the presence of structural defects in the coating allows the aggressive media to penetrate the substrates [11]. Typically, MAO is a prevalent method because of its high hardness and strong metallurgical bonding of the MAO coating to the substrates [12]. Nevertheless, the MAO-treated ceramic film is almost insulated and non-thermally conductive, resulting in overheating or charge accumulation on the Mg alloy parts used as integrated electronic devices [13]. In addition, the prepared MAO layer has a porous structure, which is incapable to provide durable corrosion protection for Mg alloys. Therefore, it is necessary to design and prepare multifunctional hybrid coatings with favorable electrical and thermal conductivity, and excellent corrosion protection properties.

Polymeric coatings have been extensively applied in metallic corrosion protection and electronic packing industries due to their excellent corrosion resistance, easy processing and applicability. Nevertheless, polymeric materials have weak bonding with metal substrates, and low thermal and electrical conductivity, which is far from satisfying the actual requirements for the devices in 5th-generation applications. Fabrication of a composite coating has been considered as a promising strategy by incorporating conductive fillers into the polymer resin. Commonly used electrically and thermally conductive fillers include metal powders [14], carbon black [15], carbon fibres (CF) [16], carbon nanotubes (CNT) [17], and antimony tin oxide (ATO) [18] together with grapheme (G) [19]. G is a two-dimensional nanomaterial with a honeycomb lattice structure, and its intrinsic electrical and thermal conductivities are up to 10^6 S/m and 5300 $W \cdot m^{-1} \cdot K^{-1}$, respectively.

In addition, the G nanosheets possess unique impermeability for obstructing corrosive media [20]. Therefore, it is of high significance for the utilization of G in the composite coating to achieve excellent electrical conductivity, thermal conductivity and corrosion resistance. The interfacial compatibility and orientation of the G layers in the coating matrix play a crucial role in the overall performance of the composite coating. To date, it is very difficult to realize the desired performance by a simply blending the randomly orientated G nanosheets in polymeric coatings.

So far, covalent and non-covalent strategies have been employed to improve the interfacial compatibility of G-based composites [21]. These methods indeed enhanced the interfacial interaction between the G layers and polymeric resin. Among them, ionic liquid (IL) has attracted wide interest due to its low toxicity, good chemical stability and strong adsorption capacity [22]. LIU et al [23] reported that IL can improve the interfacial compatibility of G in the epoxy coating through cation−π interactions with enhanced corrosion resistance. Therefore, the modification of G with IL may provide a new approach for G dispersion in resins. The natural nacre layer is composed of inorganic aragonite and organic biopolymer, with an orderly “brick and mud” layer structure [24], exhibiting excellent mechanical and impermeable properties [25]. Inspired by nacre, researchers have constructed biomimetic composites with “brick and mud” structures through LBL self-assembly [26], magnetic alignment [27], vacuum filtration [28], freeze-drying [29] and spin-coating strategies [30]. However, the approach to structural regulation in biomimetic composites is still challenging.

This study aims to fabricate a G−epoxy composite coating with biomimetic “brick and mud” structure on MAO-treated Mg alloy to achieve good thermal and electrical conductivity and excellent corrosion protection. Imidazole-based IL was first synthesized and employed to improve the interfacial interaction between the G layers and epoxy resin (EP). Besides, the orientation and existential state of G in epoxy resin were optimized with a spinning process. The “brick and mud” structure may effectively block the penetration of the aggressive medium, and improve the physical barrier performance of the coating. The oriented GI nanosheets contribute to the transportation of charges and phonons, which enhances the thermal conductivity and electrostatic dissipative properties of the coating. Therefore, the biomimetic strategy may provide a novel route for the preparation of multifunctional composite coatings.

2 Experimental

2.1 Material

The as-extruded Mg alloy AZ31 (Al 2.5−3.0 wt.%, Zn 0.7−1.3 wt.%, Mn >0.2 wt.% and the balanced Mg) was selected as the metal substrate, which was supplied by Shandong Yin Guang Yu

Yuan Light Metal Precise Forming Co., Ltd., China. The compounds such as 1-butylimidazole (AR) and 1,8-bibromooctane (AR) were purchased from Aladdin Industrial Corporation. G was obtained from Anhui Zesheng Technology Co., Ltd. (China). Bisphenol-A type epoxy resin (E-51) and corresponding waterborne amine epoxy curing agent (8538) were provided by Marine Chemical Research Institute. Sodium chloride (NaCl, AR) was obtained from Yantai Far East Fine Chemical Co., Ltd. (China). Sodium silicate ($Na_2SiO_3·9H_2O$, AR) and sodium hydroxide (NaOH, AR) were purchased from Tianjin Beichen District Fangzheng Reagent Factory (China) and Tianjin Zhiyuan Chemical Reagent Co., Ltd. (China), respectively.

2.2 Synthesis of ionic liquid (IL)

IL was synthesized based on the grafting reaction between 1-butylimidazole and 1,8-dibromooctane [23]. The mixture of 12.5 g of 1-butylimidazole and 13.6 g of 1,8-dibromooctane were put into 25 mL of ethanol to obtain a homogeneous solution, which was then transferred into a single-necked round-bottom flask. The reaction was carried out at 80 °C in an oil bath with mechanical stirring for 8 h. After cooling to room temperature, the product was obtained by removing the solvent with a rotary evaporator. The reaction diagram is shown in Fig. 1.

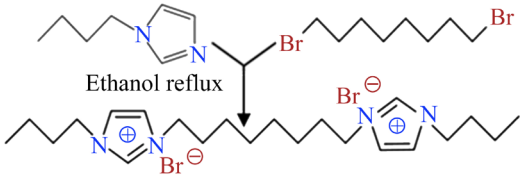

Fig. 1 Synthetic route of IL

2.3 Fabrication of IL-modified G (GI)

The G nanosheets were modified by the synthesized IL. Typically, 1 g of G was dissolved in ethanol and sonicated for 30 min to obtain a dispersion, designated as Solution A. Then, a uniform solution (Solution B) was obtained by dissolving 10 g of IL in ethanol and sonicating for 30 min. Subsequently, Solutions A and B were mixed and stirred for 1 h. After that, the precipitate was separated through centrifugation at a speed of 7000 r/min for 10 min. Finally, the product was obtained after drying in a vacuum oven (60 °C) for 12 h.

2.4 Preparation of MAO coating

The Mg alloy substrate was firstly polished to 1500 grit with SiC papers, and then washed with ethanol and deionized water. The pre-treated Mg alloy substrates were treated with an MAO process using an MAO device (HNMAO− 20A−DPM400, Xian Haoning Electronic Technology Co., Ltd., China). The equipment consisted of a power supply, a stainless-steel plate as the cathode and a stirring cooling system. The tested electrolytes were composed of 10 g/L NaOH and 18 g/L Na_2SiO_3. In the constant current mode of 1 A, the duty cycle and frequency were set at 20% and 500 Hz, respectively, and the formation process of the MAO coating required around 3 min. After the preparation of the coating, the MAO coating was rinsed with ethanol and distilled water, separately, and dried with warm air.

2.5 Fabrication of composite coatings

Composite coating was fabricated according to the following procedures. Firstly, 2 g of GI powder was dissolved in 20 mL of anhydrous ethanol and ultrasonicated to obtain a homogeneous solution, designated as Solution C, which was thoroughly mixed with 3 g of curing agent and 2 g of epoxy resin with a further 30 min of ultrasonication. In addition, the mixture was evacuated in a vacuum oven at room temperature to remove existing air bubbles. Next, the prepared resin mixture was coated on the surface of MAO-treated Mg alloy using the spin-coating method. After drying at 60 °C for 5 h, the biomimetic composite coating was prepared on the Mg alloy AZ31 substrate. To explore the arrangement of different contents of GI in the coating under the condition of spin coating, composite coatings with GI contents of 1%, 3% and 5% were prepared. To further investigate the effect of filler orientation on the performance of the composite coatings, four coatings were prepared according to the ratios in Table 1.

Table 1 Composition of composite coatings

Coating	Composition/wt.%			Method
	G	GI	Epoxy resin	
EP	−	−	100	Blending
G/EP	5	−	95	Spin-coating
GI/EP1	−	5	95	Blending
GI/EP2	−	5	95	Spin-coating

2.6 Characterization

The defects and structural variations of G and GI were investigated by Raman spectroscopy (Renishaw in Via Reflex). Besides, X-ray photoelectron spectroscopy (XPS, Thermo Scientific K-Alpha, USA) and Fourier transform infrared spectroscopy (FTIR, Nicolet 380, Thermo Electron Corporation, USA) were used to characterize the chemical structures and functional groups of G and GI. The surface morphology and cross-sectional structure of the GI/EP2 coatings were analyzed through scanning electron microscopy (FE-SEM, Nova NanoSEM 450, USA). A thermal imager (UTi260B) was used to record the surface temperature changes of coated samples. The surface resistivity and the thermal conductivity of the coating were determined via a volumetric surface area resistivity tester and the laser flash method (Netzsch, LFA457, Germany), respectively.

The corrosion resistance of the composite coatings was performed on an electrochemical workstation (CHI−660E) in 3.5 wt.% NaCl solution. A classical three-electrode cell was applied, with a working electrode (exposed area of 1 cm^2), a counter electrode (platinum plate with an area of 2.5 cm^2) and a reference electrode (saturated calomel electrode, SCE). Electrochemical impedance spectroscopy (EIS) measurement was performed in the frequency range from 10^5 to 10^{-2} Hz with a sinusoidal perturbation of 20 mV at the open circuit potential (OCP). To ensure reproducibility, three parallel-coated samples are required for all measurements. In addition, the long-term corrosion protection performance of the composite coatings was evaluated by a salt spray test according to the ASTM B117 Standard.

3 Results and discussion

3.1 Synthesis and characterization of GI

As illustrated in Fig. 1, IL was synthesized based on the grafting reaction between 1-butylimidazole and 1,8-dibromooctane. The synthesized IL was then introduced into the G surface through cation−π interactions between the imidazole ring of IL and the conjugate structure of G. And then, the GI nanomaterials were obtained.

The surface morphology and microstructure of the G and GI nanosheets are displayed in Figs. 2(a, b), respectively. The pristine G exhibited a smooth surface with fewer folds, while GI had a rougher and thicker lamellar structure. The change in G morphologies can be attributed to the wrapped IL, which indirectly indicated the successful synthesis of GI.

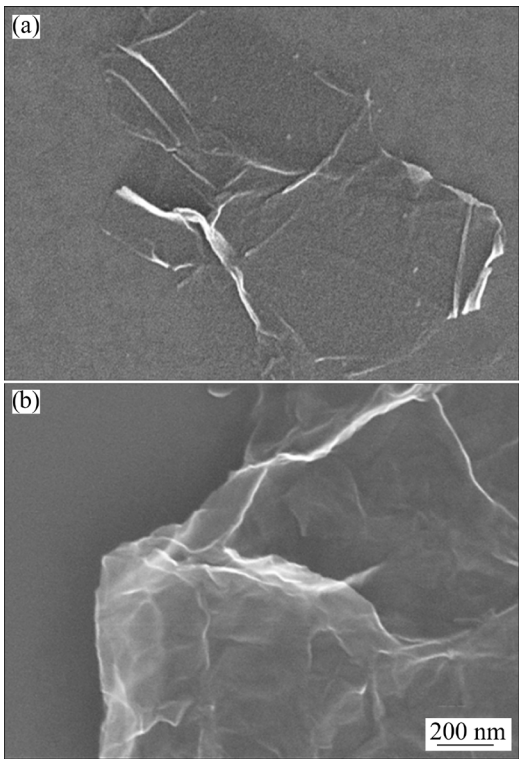

Fig. 2 SEM images of G (a) and GI (b) nanosheets

FTIR tests were conducted to detect the variations in the chemical structures of the G nanosheets during the modification process. The FTIR spectra of G, IL, and GI are displayed in Fig. 3(a). For the pristine G, the characteristic peak appeared at 1651 cm^{-1}, corresponding to the C═C stretching vibration of G six-membered rings [31,32]. Besides, the peaks at 3450 and 1084 cm^{-1} are related to the residual oxygen-containing groups in the G, prepared by the reduction−oxidation method. In contrast to the G, several new peaks were observed at 1562 and 1460 cm^{-1} in the spectrum of GI, assigning to C—N and C═N stretching vibrations, respectively. This scenario can be attributed to the imidazole rings. That is, the synthesized IL was introduced into the surface of G successfully [33,34]. In addition, the appearance of the absorption peak at 1162 cm^{-1} (in-plane asymmetric stretching vibration of imidazole) also indicated that the G was covered successfully by IL [35].

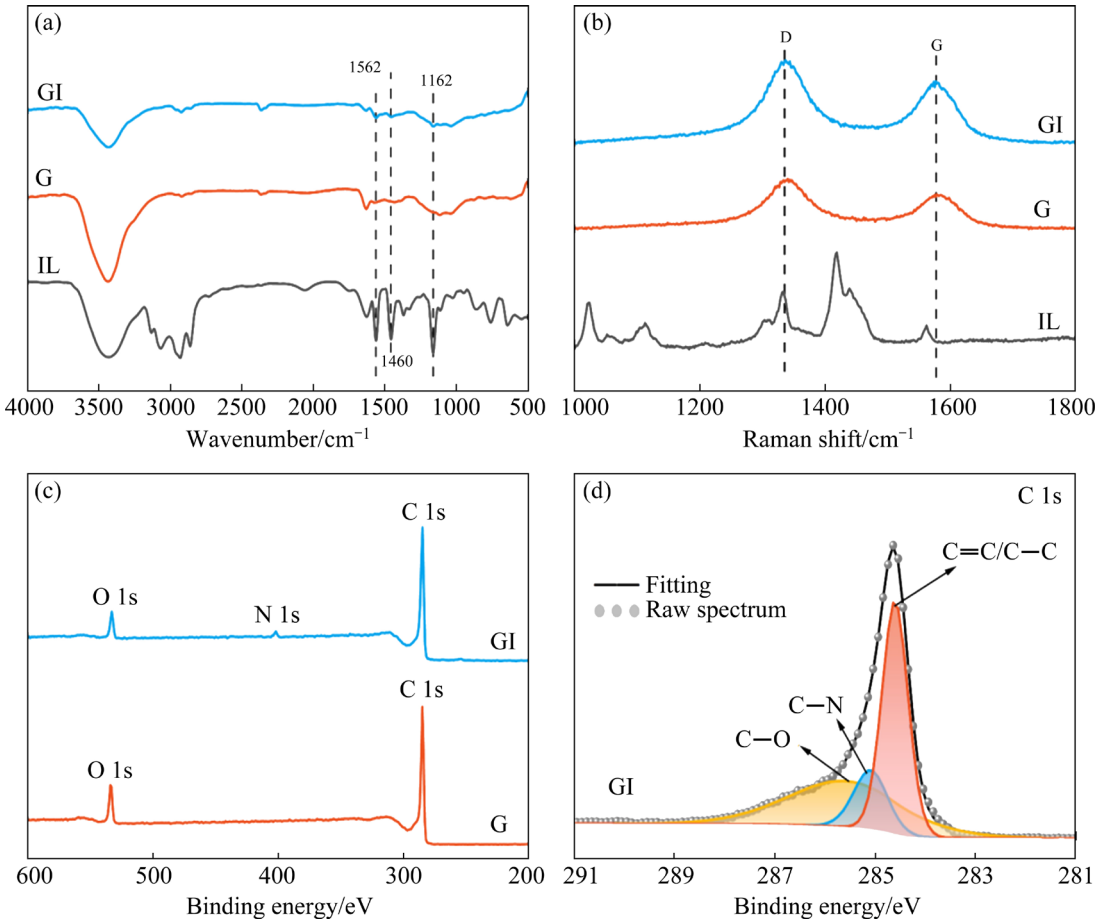

Fig. 3 FTIR (a) and Raman (b) spectra of IL, G and GI; XPS spectra of G and GI (c); C 1s XPS spectra of GI (d)

Raman spectroscopy was used to investigate the impact of IL on the G structure. As shown in Fig. 3(b), the characteristic bands of G appeared at 1340 and 1584 cm^{-1}, corresponding to D and G bands, respectively. Usually, the D band refers to the defect and disorder vibrations at the margins or planes of G [36], while the G band relates to the in-plane stretching vibrations of carbon atom sp^2 hybridization [37]. Generally, the I_D/I_G intensity ratio can be used to depict the degree of defects in G [30]. It can be observed that the modification process lowered the I_D/I_G intensity ratio. The introduced IL molecules can compensate for the defects in the G, which further suggested that IL was attached to the G surface. Additionally, the G bond shifted from 1584 to 1581 cm^{-1}, indicating the presence of the charge transfer between the G and the IL. These results further proved the presence of cation−π interactions between the G and the IL molecules [23].

The composition and chemical states of G and GI were analyzed via XPS measurements. As can be seen in Fig. 3(c), C 1s and O 1s peaks are exhibited in the spectra of the G and GI. Notably, the N peak originating from IL was found in GI [38]. The presence of N peak can be attributed to the introduced IL molecules. The high-resolution C 1s in the XPS spectra of the G and GI were presented in Figs. 3(d) and S1 in Supporting Information (SI). Compared with G, a new peak centred at 285.2 eV was observed for GI [21], ascribing to the C—N bond in the IL. The results designated that the G nanosheets were covered by the IL. In addition, only the C—N peak at 398.5 eV binding energy was detected from the N 1s spectrum of the GI, as depicted in Fig. S2 in SI. The XPS results were consistent with the FTIR and Raman results, which together confirmed that the GI was successfully synthesized.

3.2 Construction of biomimetic composites

Biomimetic composite coatings with an approximate “brick and mud” structure were constructed through the spin-coating method (Fig. 4(a)). During the spin-coating process, a centrifugal force is applied to the resin mixture,

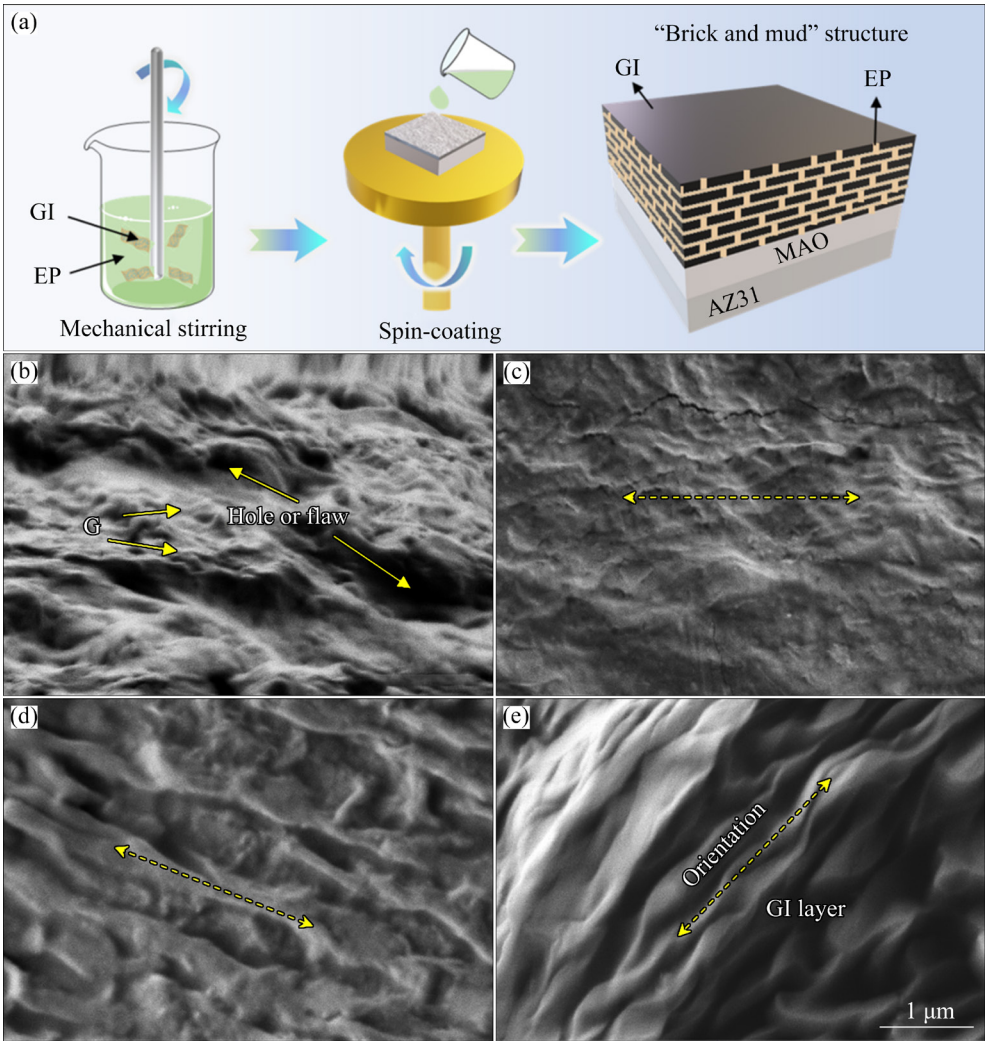

Fig. 4 Illustration for preparation of biomimetic composite coatings (a); cross-sectional morphologies of composite coatings with 5% G (b), 1% GI (c), 3% GI (d) and 5% GI (e) prepared by spin-coating method

which drives the orientation of the G layers in an epoxy resin coating. To confirm the distribution of the GI in the coating matrix, the cross-sectional morphology of the composites was investigated through SEM. Direct incorporation of the pristine G into the coating matrix without the spinning process resulted in the uneven distribution of G in the epoxy resin with a loose structure (Fig. S3 in SI). For the spin-coated unmodified G−epoxy composite coating (Fig. 4(b)), the G sheets possessed a certain orientation in the resin, while the coating presented low compactness and numerous defects. This was ascribed to the poor compatibility between the G and epoxy resin. Figure S4 in SI exhibits the SEM images and EDS mapping of the GI/EP2 coating, where the three-layer composite structure (i.e., the substrate, MAO and GI/EP2 layer) was observed with a thickness of approximately 87.3 μm. Figures 4(c−e) show cross-sectional morphologies of the composite coatings with (1%, 3% and 5%) GI, prepared by the spin-coating method. For the biomimetic composite coatings, the centrifugal force generated by high-speed rotation during the spin-coating process drove the formation of the orientation of the G and the "brick and mud" structures. Besides, the compatibility between G and epoxy resin was greatly improved as reflected by the intact and compact surfaces. The arranged G nanosheets in the composite can facilitate heat transfer and electrical conductivity in the coating [39−41]. In addition, the designed biomimetic structure can improve the impermeability of epoxy coating and thus prevent corrosion media intrusion. The thickness of the coating is displayed in Table S1 in SI.

3.3 Thermal properties of coatings

To examine the thermal transport properties of the composite coatings, the laser flash method was employed to measure the thermal diffusivity (λ). The thermal conductivity of the composite coatings is calculated based on the following formula [42]:

$$\lambda=\alpha\cdot c_p\cdot\rho \quad (1)$$

where α is the measured thermal diffusion rate, c_p is the specific heat capacity, and ρ is the measured average density.

The obtained thermal conductivities of different coatings are presented in Fig. 5(a). The thermal conductivity of EP coating was only 0.21 $W\cdot m^{-1}\cdot K^{-1}$, implying the limited capability of the epoxy coating to dissipate heat in time. With the addition of the G, the heat-conductivity of the coating significantly increased. Compared with the G/EP coating, the thermal conductivity of the GI/EP1 coating slightly increased by 0.020 $W\cdot m^{-1}\cdot K^{-1}$. However, the biomimetic composite coating (GI/EP2) displayed the highest thermal conductivity of 0.77 $W\cdot m^{-1}\cdot K^{-1}$, which was three times higher than that of the EP coating. It can be deduced that the near-parallel arranged and mutually contacted GI layers in the biomimetic structure can provide an effective heat transfer path for the composite coating.

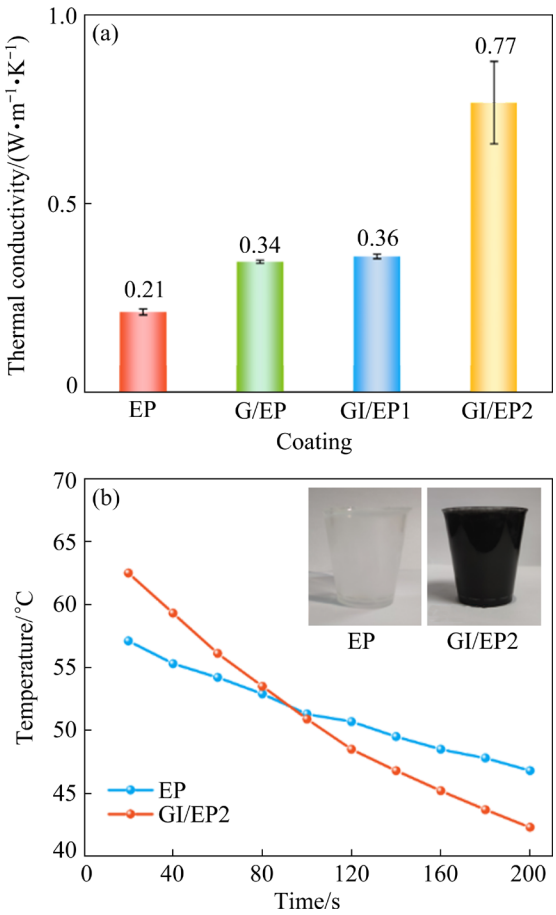

Fig. 5 Thermal conductivity of EP, G/EP, GI/EP1 and GI/EP2 coatings (a); Surface temperature of water in polystyrene cup (b)

For further evaluating the heat transfer performance of the EP and biomimetic composite coatings (GI/EP2), the temperature variations of the samples were recorded by an infrared camera during the heat dissipation test. Firstly, the EP and GI/EP2 coatings were spin-coated on the inner walls of the polystyrene cups. Subsequently, an equal amount of hot water was added to the coated cups, and the temperature variations of the water were recorded through the infrared camera from 0 to 200 s (Fig. S5 in SI). The temperature in the epoxy-coated cup decreased from 57 to 46.9 °C in 120 s. However, the temperature of the water in the biomimetic composite coated cup rapidly reduced from 62.5 to 42.4 °C in the same time duration. The phenomena demonstrated that the near-parallel arranged G in the "brick and mud" structure significantly improved the thermal dissipation performance of the coating. Figure 5(b) illustrates the optical images and temperature curve of the coated polystyrene cup. It was noticeable that the cooling curve of the biomimetic composite coating demonstrated a higher slope, indicating the faster heat conduction capacity of the biomimetic composite coating. These results are consistent with the thermal conductivity results, which reveals that the biomimetic composite coating is promising for heat transfer applications [43].

3.4 Conductive properties of coatings

Due to its superior electrical conductivity, G is applied to electrostatic dissipative materials [44]. Based on the ANSI/ESD S541-200 (USA) industry standard, materials with surface resistivity in the range from 1.0×10^4 to 1.0×10^{11} Ω·cm are classified into electrostatic dissipative materials, while surface resistivity less than 1.0×10^4 Ω·cm and greater than 1.0×10^{11} Ω·cm are categorized as conductive materials and insulating materials, respectively [45]. The surface resistivity (Fig. 6) of the EP coating was as high as 9.8×10^{11} Ω·cm, which indicated that epoxy coating belongs to insulating material [46]. The introduction of the G nanosheets into the composite coatings decreased the surface

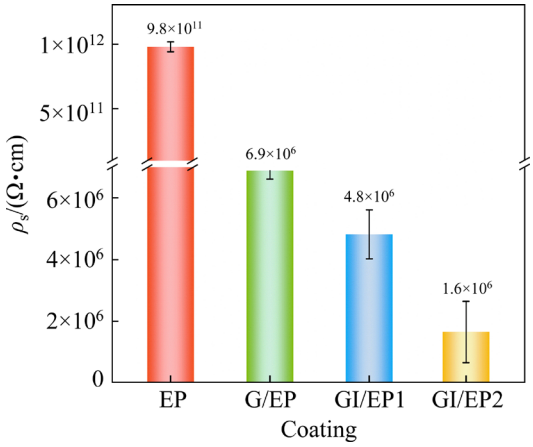

Fig. 6 Surface resistivity of EP, G/EP, GI/EP1 and GI/EP2 coatings

resistivity. After modification of the G with IL, the GI/EP1 coating displayed a lowered surface resistivity of $4.8\times10^6\ \Omega\cdot$cm, which was ascribed to the enhanced interfacial compatibility between the G sheets and the resin. Notably, the biomimetic composite coating exhibited the lowest surface resistivity ($1.6\times10^6\ \Omega\cdot$cm), demonstrating that more conductive paths were constructed by the biomimetic "brick and mud" structures.

3.5 Anti-corrosion performance of coatings

Figure 7 presents the Bode and Nyquist plots for the coated samples immersed in 3.5 wt.% NaCl solution for 40 d. Generally, the impedance value (Z) at low frequency (f=0.01 Hz) is used to estimate

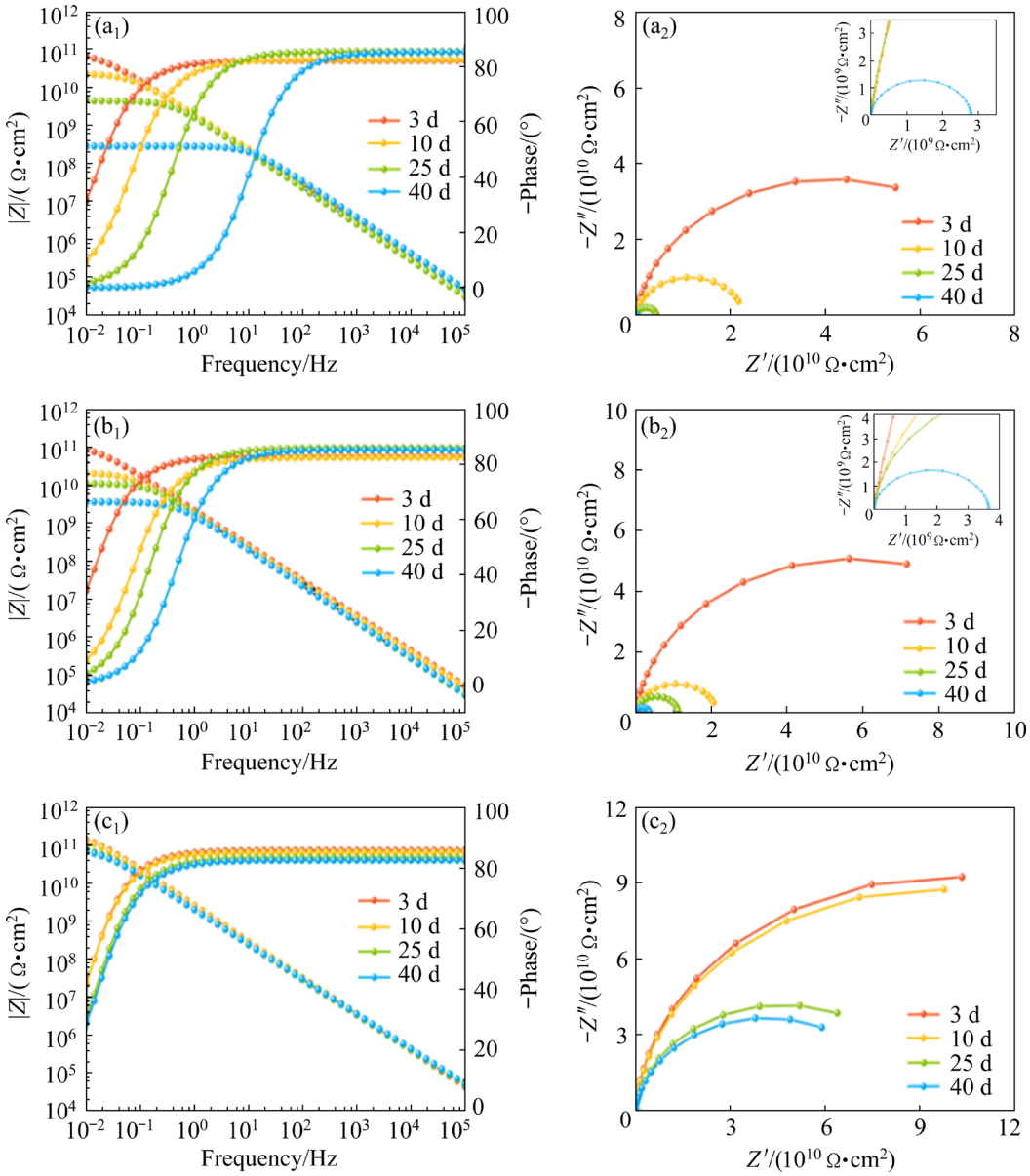

Fig. 7 Bode (a_1−c_1) and Nyquist (a_2−c_2) plots of Mg alloy substrate coated with EP (a_1, a_2), GI/EP1 (b_1, b_2), and GI/EP2 (c_1, c_2) coatings

the anticorrosion property of the coated system [47]. As can be seen, the Z value of the EP coating decreased sharply from 6.44×10^{10} to 2.80×10^{8} $\Omega\cdot cm^2$ after 40 d of soaking, indicating the rapid penetration of the aggressive ions. Compared with the EP coating, the declining extent in Z values for the GI/EP1 coating was reduced significantly. Because of the introduction of the IL, the interfacial compatibility between the G layers and the resin was improved, which increased the compactness and barrier property of the coatings. Notably, the biomimetic composite coating prepared by the spin-coating method displayed the optimum anti-corrosion performance with the highest impedance value above $10^{10}\,\Omega\cdot cm^2$ after 40 d of immersion. It can be inferred that the approximately parallel-arranged GI nanosheets in the biomimetic "brick and mud" structure effectively prevented the ingress of corrosive media. Besides, the Nyquist results were also consistent with the Bode plots. Usually, a larger capacitance arc indicates better corrosion resistance of coating [48]. It was evident that the capacitance arcs of the epoxy coating reduced rapidly during the immersion period, revealing the unsatisfactory corrosion protection capability. Larger capacitance arcs exhibited for the GI/EP coating, compared with the EP coating. However, the biomimetic composite coating showed the largest capacitance arc during the whole immersion period, which illustrated that the biomimetic composites prepared by spin-coating obtained superior impermeability and excellent corrosion protection performance.

To better analyze the corrosion process of the composite coatings, the EIS results were further fitted by ZSimpWin software using the corresponding equivalent circuits in Fig. 8, and the corresponding fitted data are presented in Table S2 in SI. Generally, R_s and R_c represent the resistances of the solution and the coating, respectively. Owing to the dispersion effect [49], the interfacial capacitance was represented by a constant phase element, CPE (Q_c denotes the coating capacitance). Usually, the coating resistance to aggressive species can be reflected by R_c values [50]. The fitted R_c results for the coating as a function of time are shown in Fig. S6 in SI. As the immersion time extended, the R_c values for each coating system gradually decreased. Especially, during the entire testing process, the biomimetic composite coating with a "brick and mud" structure displayed the highest R_c values, revealing its superior barrier property.

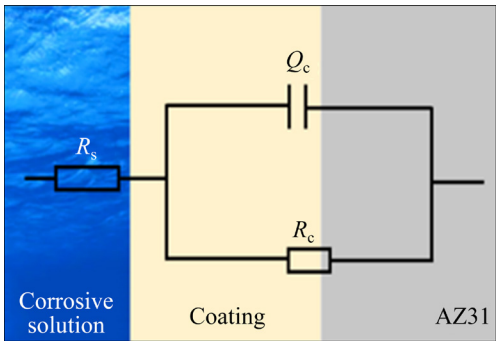

Fig. 8 Equivalent circuit model of EIS data

Moreover, the breakpoint frequency (f_b), the frequency at −45° in the phase angle, is another valid parameter for verifying the protective properties of coatings because f_b is closely related to the microscopic delamination of the coating [51]. The change in f_b for all coatings over 45 d of immersion is displayed in Fig. 9. The increase in f_b values can be attributed to interfacial corrosion, which can weaken the forces between the metal and coating and result in coating deterioration. The variations of f_b values are negligible for biomimetic composites during 40 d of immersion, indicating that the interfacial corrosion has been greatly inhibited. These phenomena confirmed that the oriented GI in the "brick and mud" structure obviously suppressed the penetration of electrolytes and prevented the coating delamination.

To verify the actual corrosion protection performance of the prepared coating, salt spray tests

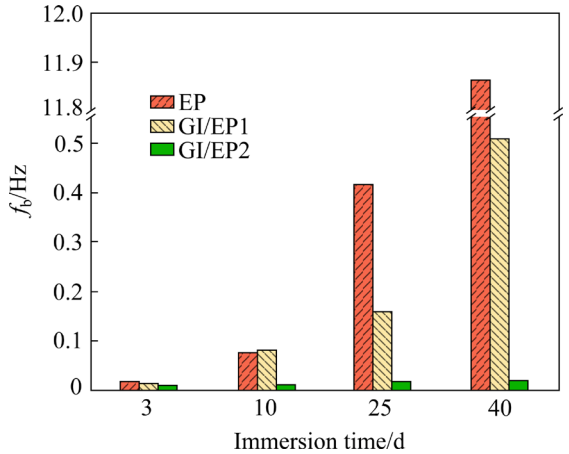

Fig. 9 Breakpoint frequency (f_b) for different coating systems during immersion

were conducted. Before the test, the coating was manually scribed with a surgical knife to expose the metal substrate to the solution. Then, the damaged coating was placed in a test chamber with continuous spray (5 wt.% NaCl solution) at (35±2) °C. Figure 10 presents the images of the composite coatings during 240 h of the test. The corrosion products in Fig. 10(a) were found in the scratched area after 24 h. Besides, obvious corrosion pits appeared on the surrounding area of the EP coating, illustrating the rapid deterioration of EP coating. As the test time extended, large amounts of corrosion products filled the scratches accompanied by coating bulging. The observations indicated the poor protection performance of the EP coating. As for the biomimetic composite coating in Fig. 10(b), the corrosion products in the scratched area were detected after 120 h. Moreover, no visible defects and corrosion pits exhibited during 240 h of the test, which demonstrated the excellent protection performance of the Mg alloy substrate.

In order to investigate the extent of corrosion after salt spray measurement, the corrosion morphology and elemental compositions of the scratched areas were analyzed through SEM and EDS. Compared with the EP coating (Fig. 11(a)), the biomimetic composite coating (Fig. 11(b)) exhibited fewer corrosion products in the crevices. As can be seen from the EDS results, a high concentration of Na and Cl elements was observed at the scratches on the EP coating, which proved the

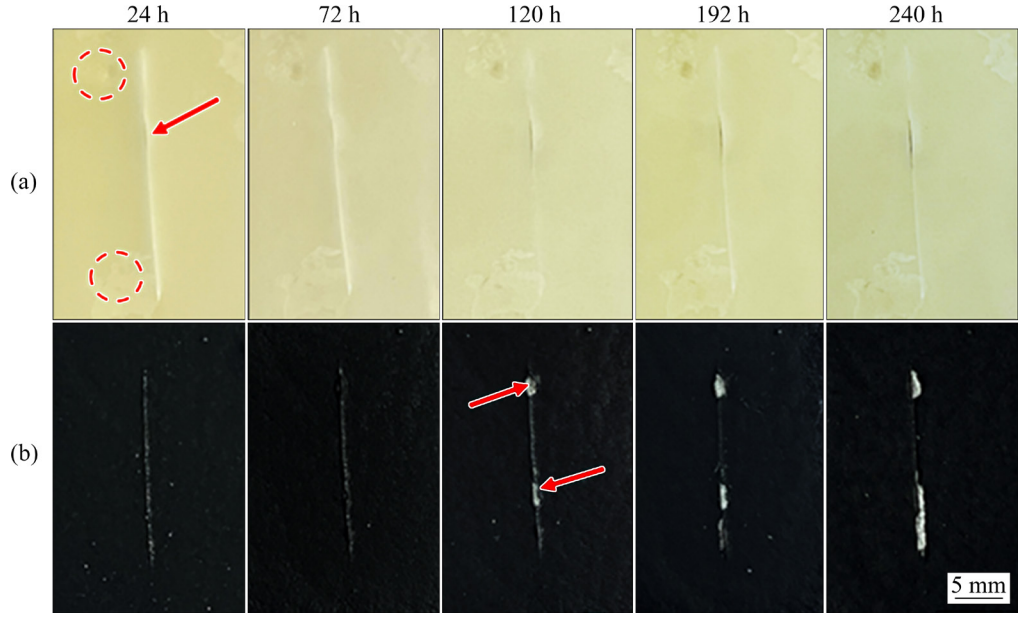

Fig. 10 Visual performance of EP (a) and GI/EP2 (b) coatings after 240 h of salt spray test

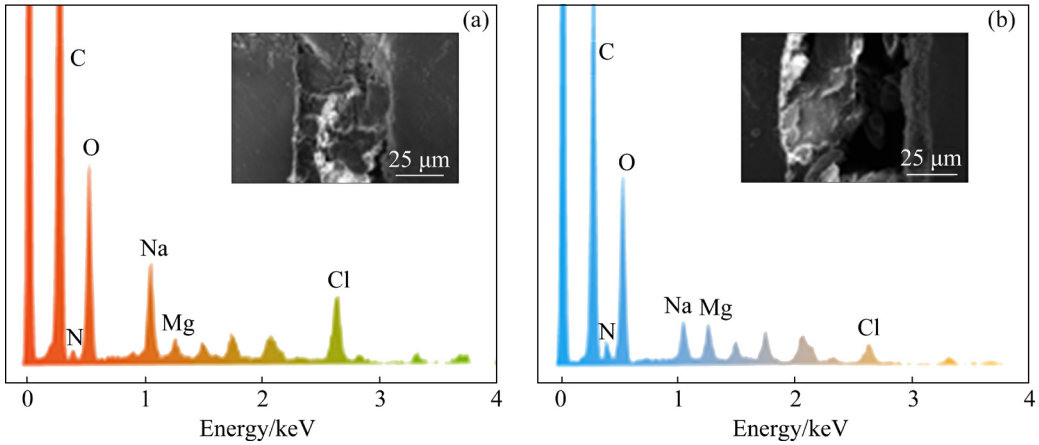

Fig. 11 SEM images and EDS analysis results of different scratched coatings after salt spray for 240 h: (a) EP; (b) GI/EP2

severe corrosion of the exposed Mg substrate. Significantly, the EDS results for the biomimetic composite coating remained in the low range for Na and Cl elements. These results confirmed that the approximately parallel aligned G nanosheets in the "brick and mud" structure can extend the intrusion path of the electrolyte, hence retarding the corrosion of the Mg substrate.

3.6 Synergistic mechanism of heat conduction, electricity conduction and corrosion protection of composite coatings

The specific working mechanism is illustrated in Fig. 12. For a composite coating, the interfacial compatibility between the filler and the resin, and the orientation of the filler in the resin played significant roles in the overall performance of the coating system. Firstly, IL was synthesized and introduced into the G surface to improve the dispersion of G in the resin. Subsequently, the spin-coating method endowed the biomimetic composite coating with a "brick and mud" structure, in which the GI layers were approximately arranged in parallel. The orientated GI nanosheets effectively reduced phonon scattering and facilitated the formation of heat transfer paths, which improved heat transfer efficiency. Normally, the accumulation of static charges could produce a discharge phenomenon, which could result in fire and explosion accidents. The nearly parallel arranged GI nanosheets contributed to the generation of conductive pathways, enhancing the electrostatic dissipative property.

Generally, the barrier property of anticorrosion coatings is crucial in practical applications. Due to the limited barrier capacity of the pure epoxy coating, the corrosive media (O_2, H_2O and Cl^-) would rapidly penetrate into the coating and induce metal corrosion. The orientation and distribution state of the filler exerted a major influence on the barrier property of the organic coating. Importantly, the GI layers in the "brick and mud" structure prepared by the spin-coating method presented near-parallel orientation, which greatly prevented the penetration of aggressive species and achieved long-term corrosion resistance. Therefore, the multifunctional coating with superior thermal conductivity, electrostatic dissipation and anti-corrosion properties was prepared by the spin-coating method.

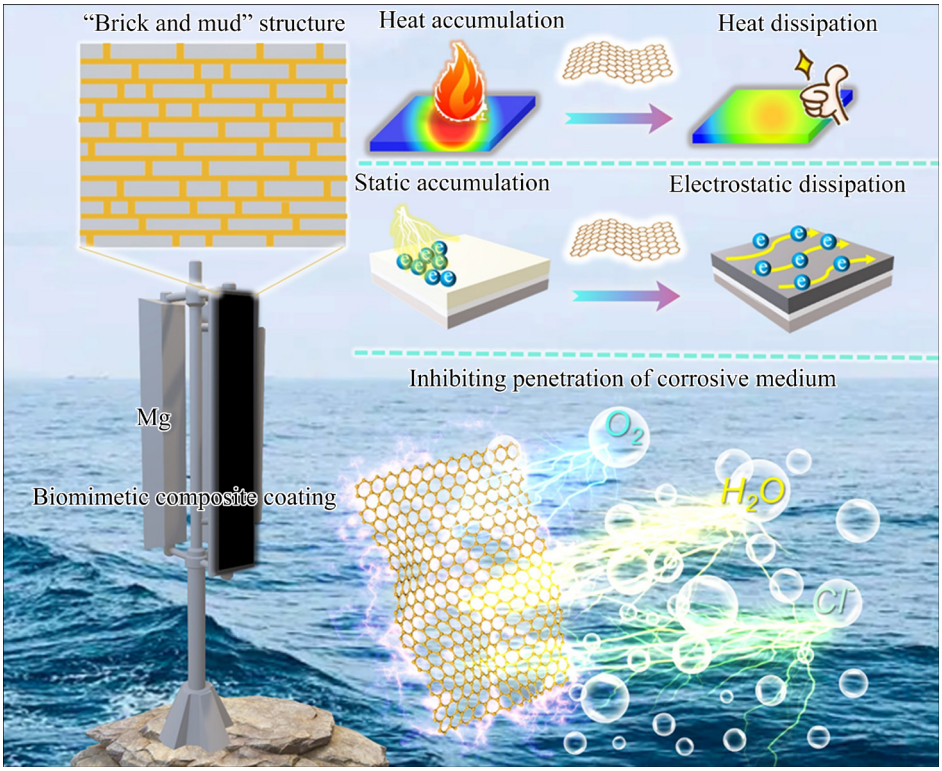

Fig. 12 Schematic diagram of mechanism of heat conduction, electricity conduction and corrosion protection of multifunctional coating

4 Conclusions

(1) The interfacial compatibility between the G nanosheets and the resin coating was dramatically improved by the presence of the IL on the G surface. Fracture surface morphology investigations indicated that the pin-holes and defects in the coating were successfully reduced, contributing to the enhanced density of the coating.

(2) Compared with the pure epoxy coating, the thermal conductivity of biomimetic composite coating with a “brick and mud “structure increased by two times, and the biomimetic composite coating displayed the optimal heat dissipation capacity in thermal tests. The oriented GI nanosheets in the “brick and mud” structure promoted charge transfer and contributed to the reduction of the surface resistivity of the coating ($1.6\times10^6\,\Omega\cdot$cm), demonstrating the favourable electrostatic dissipative properties of the coating.

(3) Electrochemical and salt spray results demonstrated that the biomimetic composite coating possessed an improved corrosion resistance with an impedance value of $6.76\times10^{10}\,\Omega\cdot\text{cm}^2$. Multifunctional composite coatings based on biomimetic strategies are expected to be applied in complex and harsh environments.

CRediT authorship contribution statement

Pu-sheng SUI: Investigation, Methodology, Writing − Original draft; **Cheng-bao LIU:** Supervision, Conceptualization, Funding acquisition, Writing − Review & editing; **Ai-meng ZHANG:** Investigation, Methodology; **Cong SUN:** Investigation, Methodology; **Lan-yue CUI:** Investigation, Methodology; **Rong-chang ZENG:** Supervision, Funding acquisition, Writing − Review & editing.

Declaration of competing interest

There are no conflicts of interest to declare.

Acknowledgments

The authors gratefully appreciate the financial support of the National Natural Science Foundation of China (Nos. 52071191, 52201077), the Natural Science Foundation of Shandong Province, China (No. ZR2022QE191), and Talent Introduction and Research Start-up Fund of Shandong University of Science and Technology, China (No. 0104060510124).

Supporting Information

Supporting Information in this paper can be found at: http://tnmsc.csu.edu.cn/download/10-p0157-2022-1109-Supporitng_Information.pdf.

References

[1] YAN C J, XIN Y C, CHEN X B, XU D K, CHU P K, LIU C Q, GUAN B, HUANG X X, LIU Q. Evading strength−corrosion tradeoff in Mg alloys via dense ultrafine twins [J]. Nature Communications, 2021, 12: 4616.

[2] XIN T Z, ZHAO Y H, MAHJOUB R, JIANG J X, YADAV A, NOMOTO K, NIU R M, TANG S, JI F, QUADIR Z, MISKOVIC D, DANIELS J, XU W Q, LIAO X Z, CHEN L Q, HAGIHARA K, LI X Y, RINGER S, FERRY M. Ultrahigh specific strength in a magnesium alloy strengthened by spinodal decomposition [J]. Science Advances, 2021, 7: eabf3039.

[3] NEZAMDOUST S, SEIFZADEH D. Application of CeH-V/sol−gel composite coating for corrosion protection of AM60B magnesium alloy [J]. Transactions of Nonferrous Metals Society of China, 2017, 27: 352−362.

[4] ZHANG A M, LENIN P, ZENG R C, KANNAN M B. Advances in hydroxyapatite coatings on biodegradable magnesium and its alloys [J]. Journal of Magnesium and Alloys, 2022, 10: 1154−1170.

[5] van PHUONG N, GUPTA M, MOON S. Enhanced corrosion performance of magnesium phosphate conversion coating on AZ31 magnesium alloy [J]. Transactions of Nonferrous Metals Society of China, 2017, 27: 1087−1095.

[6] CHEN Y N, WU L, YAO W H, WU J H, XIANG J P, DAI X W, WU T, YUAN Y, WANG J F, JIANG B, PAN F S. Development of metal-organic framework (MOF) decorated graphene oxide/MgAl-layered double hydroxide coating via microstructural optimization for anti-corrosion micro-arc oxidation coatings of magnesium alloy [J]. Journal of Materials Science & Technology, 2022, 130: 12−26.

[7] HE L J, SHAO Y, LI S Q, CUI L Y, JI X J, ZHAO Y B, ZENG R C. Advances in layer-by-layer self-assembled coatings upon biodegradable magnesium alloys [J]. Science China Materials, 2021, 64: 2093−2106.

[8] RAJABALIZADEH Z, SEIFZADEH D, KHODAYARI A, SOHRABNEZHAD Sh. Corrosion protection and mechanical properties of the electroless Ni−P−MOF nanocomposite coating on AM60B magnesium alloy [J]. Journal of Magnesium and Alloys, 2022, 10: 2280−2295.

[9] NEZAMDOUST S, SEIFZADEH D, HABIBI-YANGJEH A. Nanodiamond incorporated sol−gel coating for corrosion protection of magnesium alloy [J]. Transactions of Nonferrous Metals Society of China, 2020, 30: 1535−1549.

[10] ABDI-ALGHANAB K, SEIFZADEH D, RAJABALIZADEH Z, HABIBI-YANGJEH A. High corrosion protection performance of the LDH/Ni-P composite coating on AM60B magnesium alloy [J]. Surface and Coatings Technology, 2020, 397: 125979.

[11] LIU A H, XU J L. Preparation and corrosion resistance of superhydrophobic coatings on AZ31 magnesium alloy [J]. Transactions of Nonferrous Metals Society of China, 2018,

28: 2287−2293.

[12] CAI L, SONG X, LIU C B, CUI L Y, LI S Q, ZHANG F, BOBBY KANNAN M, CHEN D C, ZENG R C. Corrosion resistance and mechanisms of $Nd(NO_3)_3$ and polyvinyl alcohol organic-inorganic hybrid material incorporated MAO coatings on AZ31 Mg alloy [J]. Journal of Colloid and Interface Science, 2023, 630: 833−845.

[13] LI T, LENG Z J, WANG X T, WANG S F, ZHANG S Q, YANG Y S, ZHOU J X. Microstructure and electrical conductivity of electroless copper plating layer on magnesium alloy micro-arc oxidation coating [J]. Transactions of Nonferrous Metals Society of China, 2022, 32: 3950−3962.

[14] MIRMOHSENI A, RASTGAR M, OLAD A. Effectiveness of PANI/Cu/TiO ternary nanocomposite on antibacterial and antistatic behaviors in polyurethane coatings [J]. Journal of Applied Polymer Science, 2020, 137: 48825.

[15] CIARDIELLO R, DRZAL L T, BELINGARDI G. Effects of carbon black and graphene nano-platelet fillers on the mechanical properties of syntactic foam [J]. Composite Structures, 2017, 178: 9−19.

[16] KIM J, CHA J, CHUNG B J, RYU S, HONG S H. Fabrication and mechanical properties of carbon fiber/epoxy nanocomposites containing high loadings of noncovalently functionalized graphene nanoplatelets [J]. Composites Science and Technology, 2020, 192: 108101.

[17] LIU Y, HE D L, DUBRUNFAUT O, ZHANG A N, ZHANG H L, PICHON L, BAI J B. GO-CNTs hybrids reinforced epoxy composites with porous structure as microwave absorbers [J]. Composites Science and Technology, 2020, 200: 108450.

[18] WANG T, GE H Y, ZHANG K L. A novel core-shell silica@graphene straticulate structured antistatic anticorrosion composite coating [J]. Journal of Alloys and Compounds, 2018, 745: 705−715.

[19] MUNOZ-GUIJOSA J M, FERNÁNDEZ Z G, PEÑA-RODRÍGUEZ O, AKASAKA H. Toughening of graphene oxide-epoxy nanocomposites by means of very high pressures and shear rates [J]. Composites Science and Technology, 2020, 199: 108354.

[20] ZHANG Y, TIAN J W, ZHONG J, SHI X M. Thin nacre-biomimetic coating with super-anticorrosion performance [J]. ACS Nano, 2018, 12: 10189−10200.

[21] LIU C B, DU P, ZHAO H C, WANG L P. Synthesis of L-histidine-attached graphene nanomaterials and their application for steel protection [J]. ACS Applied Nano Materials, 2018, 1: 1385−1395.

[22] GAN C L, LIANG T, LI W, FAN X Q, ZHU M H. Amine-terminated ionic liquid modified graphene oxide/copper nanocomposite toward efficient lubrication [J]. Applied Surface Science, 2019, 491: 105−115.

[23] LIU C B, DU P, NAN F, ZHAO H C, WANG L P. Dual functions of imidazole-based polymeric ionic liquid (PIL) on the anticorrosive performance of graphene-based waterborne epoxy coatings [J]. Surface Topography: Metrology and Properties, 2018, 6: 024004.

[24] CHENG Q F, JIANG L, TANG Z Y. Bioinspired layered materials with superior mechanical performance [J]. Accounts of Chemical Research, 2014, 47: 1256−1266.

[25] DING J H, ZHAO H R, YU H B. Superior and durable graphene-based composite coatings by bioinspired interfaces and alignment [J]. Composites Science and Technology, 2021, 214: 108967.

[26] WAN S J, JIANG L, CHENG Q F. Design principles of high-performance graphene films: Interfaces and alignment [J]. Matter, 2020, 3: 696−707.

[27] LIN F, ZHU Z, ZHOU X F, QIU W L, NIU C, HU J, DAHAL K, WANG Y N, ZHAO Z H, REN Z F, LITVINOV D, LIU Z P, WANG Z M M, BAO J M. Orientation control of graphene flakes by magnetic field: Broad device applications of macroscopically aligned graphene [J]. Advanced Materials, 2016, 29: 1604453.

[28] HOU H, DAI W, YAN Q W, LV L, ALAM F E., YANG M H, YAO Y G, ZENG X L, XU J B, YU J H, JIANG N, LIN C T. Graphene size-dependent modulation of graphene frameworks contributing to the superior thermal conductivity of epoxy composites [J]. Journal of Materials Chemistry A, 2018, 6: 12091−12097.

[29] PENG J S, HUANG C J, CAO C, SAIZ E, DU Y, DOU S X, TOMSIA A P, WAGNER H D, JIANG L, CHENG Q F. Inverse nacre-like epoxy-graphene layered nanocomposites with integration of high toughness and self-monitoring [J]. Matter, 2020, 2: 220−232.

[30] CHU J H, TONG L B, WEN M, JIANG Z H, ZOU D N, LIU S F, ZHANG H J. Inhibited corrosion activity of biomimetic graphene-based coating on Mg alloy through a cerium intermediate layer [J]. Carbon, 2020, 161: 577−589.

[31] LUO J, ZHAO F Q, FEI X M., LIU X Y, LIU J C. Mussel inspired preparation of polymer grafted graphene as a bridge between covalent and noncovalent methods [J]. Chemical Engineering Journal, 2016, 293: 171−181.

[32] CHU J H, TONG L B, ZHANG J B, KAMADO S, JIANG Z H, ZHANG H J, SUN G X. Bio-inspired graphene-based coatings on Mg alloy surfaces and their integrations of anti-corrosive/wearable performances [J]. Carbon, 2019, 141: 154−168.

[33] WANG H, ZHANG H, ZHANG J H, ZHAO Y F. Improving tribological performance of fluoroether rubber composites by ionic liquid modified graphene [J]. Composites Science and Technology, 2019, 170: 109−115.

[34] SARATH P S, MAHESH T Y, PANDEY M K, HAPONIUK J T, THOMAS S, GEORGE S C. Tribological performance of ionic liquid modified graphene oxide/silicone rubber composite and the correlation of properties using machine learning methods [J]. Polymer Engineering and Science, 2022, 62: 1473−1484.

[35] LYU Q, YAN H X, LI L, CHEN Z Y, YAO H H, NIE Y F. Imidazolium ionic liquid modified graphene oxide: As a reinforcing filler and catalyst in epoxy resin [J]. Polymers, 2017, 9: 447.

[36] FU W, WANG L, LUO J L, DENG J Y, LIU Q W. Dodecylbenzene-modified graphite oxide via π−π interaction to reinforce EPDM [J]. Journal of Applied Polymer Science, 2019, 136: 48261.

[37] WEN S F, MA J C. Synergistic effect of polyvinyl-pyrrolidone noncovalently modified graphene and epoxy resin in anticorrosion application [J]. High Performance Polymers, 2021, 33: 146−164.

[38] WAN S J, HU H, PENG J S, LI Y C, FAN Y Z, JIANG L, CHENG Q F. Nacre-inspired integrated strong and tough reduced graphene oxide-poly (acrylic acid) nanocomposites [J]. Nanoscale, 2016, 8: 5649−5656.
[39] VERMA M, VERMA P, DHAWAN S K, CHOUDHARY V. Tailored graphene based polyurethane composites for efficient electrostatic dissipation and electromagnetic interference shielding applications [J]. RSC Advances, 2015, 5: 97349−97358.
[40] CHEN C, XUE Y, LI Z, WEN Y F, LI X W, WU F, LI X J, SHI D A, XUE Z G, XIE X L. Construction of 3D boron nitride nanosheets/silver networks in epoxy-based composites with high thermal conductivity via in-situ sintering of silver nanoparticles [J]. Chemical Engineering Journal, 2019, 369: 1150−1160.
[41] BAO D, GAO Y Y, CUI Y X, XU F, SHEN X S, GENG H L, ZHANG X G, LIN D, ZHU Y J, WANG H Y. A novel modified expanded graphite/epoxy 3D composite with ultrahigh thermal conductivity [J]. Chemical Engineering Journal, 2022, 433: 133519.
[42] ZHANG F, YE C, DAI W, LV L, YUAN Q L, CHEE K W A, YANG K, JIANG N, LIN C T, ZHAN Z L, DAI D, LI H. Surfactant-assisted fabrication of graphene frameworks endowing epoxy composites with superior thermal conductivity [J]. Chinese Chemical Letters, 2020, 31: 244−248.
[43] DING J H, ZHAO H R, YU H B. Bio-inspired multifunctional graphene-epoxy anticorrosion coatings by low-defect engineered graphene [J]. ACS Nano, 2022, 16: 710−720.
[44] MENG Q S, YU Y, TIAN J Y, YANG Z K, GUO S, CAI R, HAN S S, LIU T Q, MA J. Multifunctional, durable and highly conductive graphene/sponge nanocomposites [J]. Nanotechnology, 2020, 31: 465502.
[45] GAO W, DANG Z C, LIU F S, WANG S, ZHANG D W, YAN M X. Preparation of antistatic epoxy resin coatings based on double comb-like quaternary ammonium salt polymers [J]. RSC Advances, 2020, 10: 43523−43532.
[46] GUO B B, JI X Z, WANG W, CHEN X T, WANG P, WANG L P, BAI J M. Highly flexible, thermally stable, and static dissipative nanocomposite with reduced functionalized graphene oxide processed through 3D printing [J]. Composites Part B: Engineering, 2021 208: 108598.
[47] CUI M J, REN S M, ZHAO H C, XUE Q J, WANG L P. Polydopamine coated graphene oxide for anticorrosive reinforcement of water-borne epoxy coating [J]. Chemical Engineering Journal, 2018, 335: 255−266.
[48] HINDERLITER B R, CROLL S G, TALLMAN D E, SU Q, BIERWAGEN G P. Interpretation of EIS data from accelerated exposure of coated metals based on modeling of coating physical properties [J]. Electrochimica Acta, 2006, 51: 4505−4515.
[49] ALEXANDER C L, TRIBOLLET B, ORAZEM M E. Contribution of surface distributions to constant-phase-element (CPE) behavior: 1. Influence of roughness [J]. Electrochimica Acta, 2015, 173: 416−424.
[50] SHAKER M, SALAHINEJAD E, CAO Wei-qi, MENG X M, ZAHEDI A V, GE Qi. The effect of graphene orientation on permeability and corrosion initiation under composite coatings [J]. Construction and Building Materials, 2022, 319: 126080.
[51] RAMEZANZADEH B, NIROUMANDRAD S, AHMADI A, MAHDAVIAN M, MOGHADAM M H M. Enhancement of barrier and corrosion protection performance of an epoxy coating through wet transfer of amino functionalized graphene oxide [J]. Corrosion Science, 2016, 103: 283−304.

通过调控表面石墨烯–环氧树脂复合涂层的仿生界面和取向以提高镁合金的防腐和热/电性能

隋普升[1]，刘成宝[1]，张爱猛[1]，孙 聪[1]，崔蓝月[1]，曾荣昌[1,2]

1. 山东科技大学 材料科学与工程学院，青岛 266590；
2. 郑州大学 材料科学与工程学院，郑州 450002

摘 要：通过旋涂方法制备具有“砖泥”结构的仿生石墨烯–环氧树脂复合涂层。合成咪唑基离子液体修饰的石墨烯(GI)以改善石墨烯(G)和环氧树脂之间的界面相容性。通过扫描电镜、拉曼光谱、X 射线光电子能谱和傅里叶变换红外光谱观察和分析其表面形貌和化学结构，利用热成像仪记录表面温度变化，通过体积表面积电阻率测试仪和激光闪点法分别测定涂层的表面电阻率和导热系数，通过电化学阻抗谱和盐雾腐蚀试验表征其耐蚀性。复合涂层中的 GI 层呈现出近似平行的取向，从而提高热传导和静电耗散效率。穿过平面的导热系数和表面电阻率分别为 0.77 $W·m^{-1}·K^{-1}$ 和 $1.6×10^6$ Ω·cm。电化学阻抗谱测试表明，经过 40 d 的浸泡，涂层的低频模量达到 $6.76×10^{10}$ Ω·cm^2，比纯环氧涂层提高约 2 个数量级，表现出优异的耐腐蚀性。

关键词：仿生结构；复合涂层；镁合金；石墨烯取向；耐蚀性

(Edited by Bing YANG)